Scilight

Remediation Ecology

https://www.sciltp.com/journals/re



Article

Coupling Low-Sized Humic Acid with High Flow Rate to Increase the Mobility of CMC-Stabilized Zero-Valent Iron Nanoparticles in Iron Oxide-Coated Porous Media

Tongju Cui [1,†], Yan Wang [2,†] and Xinyao Yang [1,*]

[1] Key Laboratory of Eco-Restoration of Regional Contaminated Environment, Ministry of Education, Shenyang 110044, China
[2] The First Geological Exploration Institute of China Metallurgical Geology Administration, Langfang 065201, China
* Correspondence: xinyao.yang@syu.edu.cn
† These authors contributed equally to this work.

How To Cite: Cui, T.; Wang, Y.; Yang, X. Coupling Low-Sized Humic Acid with High Flow Rate to Increase the Mobility of CMC-Stabilized Zero-Valent Iron Nanoparticles in Iron Oxide-Coated Porous Media. *Remediation Ecology* **2026**, *1*(1), 7. https://doi.org/10.53941/re.2026.100007

Received: 1 September 2026
Revised: 8 October 2026
Accepted: 19 October 2026
Published: 26 October 2026

Abstract: Limited mobility in saturated porous media remains a critical bottleneck constraining the widespread application of engineered nanoparticles in groundwater remediation. This study demonstrates that co-injecting humic acid (HA) with nanoscale zero-valent iron (NZVI), a widely used nanoremediation agent, markedly enhances NZVI mobility, and this enhancement is further amplified by using a lower HA size and higher flow rate. Compared with higher-sized HA (<1 μm), the use of lower-sized HA (<0.1 μm) increased the maximum transport distance (L_T) of NZVI by 70%, from 23 to 39 cm. Increasing the flow rate from 1 to 2 mL min^{-1} likewise increased L_T by 78%, from 23 to 41 cm. Statistical analysis further showed that the size of HA exerted a stronger control than the flow rate (|ME| = 0.33 vs. 0.16), whereas the interaction between the two factors was negligible (IF = −0.03). Accordingly, the particle-to-HA size ratio is proposed as a quantitative metric for the mobility-enhancing effect of HA, with a larger ratio corresponding to a greater enhancement. These findings provide a preliminary strategy for overcoming the limited mobility of NZVI in saturated porous media.

Keywords: zero-valent iron nanoparticle; mobility enhancement; humic acid co-injection; size effect; flow rate effect; saturated porous media

1. Introduction

Nanoscale zero-valent iron (NZVI) has been widely applied in the *in situ* remediation of contaminated groundwater because of its high specific surface area, reducing activity, and degradation capacity [1–3]. Nevertheless, due to adsorption by granule bed, the effective transport distances of NZVI in groundwater aquifers typically only reach several to several tens of centimeters [4,5]. The limited mobility in the porous media hinders engineered application of the NZVI for contaminated site remediation [6,7].

Various surface-modification strategies have been developed to improve the mobility of NZVI. Some widely-used surface modifiers include carboxymethyl cellulose (CMC), polyacrylic acid (PAA), polyvinylpyrrolidone (PVP) and guar gum [8]. These polymer layers could effectively stabilize NZVI via electrostatic, steric, or electro-steric repulsions [9–12]. Despite the improved stability, nanoparticle mobility cannot be secured due to the attenuation of the particles by granular beds in groundwater aquifers. Aquifer sand grains typically carry iron, manganese, aluminum, and various other oxide minerals in the surface [13,14]. Under the near-neutral pH conditions typical of groundwater, the metal oxides are usually positively or weakly negatively charged and function as effective sites for the negatively charged CNZVI [15,16]. Chen et al. [17] stated that even a small amount of iron oxide coating on quartz sand increased the NZVI deposition coefficient (K_d) by several folds and



Copyright: © 2026 by the authors. This is an open access article under the terms and conditions of the Creative Commons Attribution (CC BY) license (https://creativecommons.org/licenses/by/4.0/).
Publisher's Note: Scilight stays neutral with regard to jurisdictional claims in published maps and institutional affiliations.

substantially shortened its transport distance. Thus, a potential strategy to increase NZVI mobility is to reduce their deposition rate by blocking the deposition sites (i.e., iron oxide coatings) on mineral surfaces.

Our previous studies demonstrate that natural organic matter (NOM) such as humic acid (HA) could effectively block the deposition of negatively charged particles including polystyrene microspheres [16,18–20]. This implies that HA may also be a suitable material to block the deposition of NZVI. Although the site blockage increases with increasing amount of HA injection [16], excessive input of HA into groundwater is not environmentally-friendly due to its consumption of oxidants, passivation of NZVI, and induction of bioclogging [21–25].

Our another study indicate that manipulating pH and IS could change the site blocking efficiency of HA: high pH and low IS could increase the HA blockage [18]. This implies that the amount of HA used could be minimalized by optimizing pH and IS. However, this requires significant perturbation of water chemistry which is ecologically undesired. Our more recent study shows that HA has a stronger site blockage on larger particles and such effect increases with increasing flow rate [20]. This implies that by manipulating physical parameters such as particle size and flow rate, the HA efficiency could also be promoted. In the previous study, the blocking efficiency was enhanced by increasing the particle size of microspheres; nonetheless, this approach may be constrained in engineering practice by the pore size limitations of porous media, which preclude the use of large-sized NZVI. Given that enlarging microsphere particle size increased the particle size ratio of microspheres to HA, we hypothesized that an increase in this ratio, achieved by reducing HA size, would also promote HA blockage.

To verify the above hypothesis, column tests using a widely-used CMC-NZVI and three different HA size fractions (1, 0.45, and 0.1 μm), respectively representing colloidal, dissolved and nanoscale HA, were performed using the experimental protocol developed previously [20]. Specifically, we aim to address the following questions: (1) To verify the hypothesis that the site blocking efficiency of HA would be enhanced with lower-sized HA; (2) To quantify the statistical importance of HA size and flow rate as well as their interactions on the NZVI site blockage by HA.

2. Materials and Methods

2.1. CNZVI Particles

Carboxymethyl cellulose-stabilized nanoscale zero-valent iron (CNZVI) was synthesized via liquid-phase reduction of $FeSO_4 \cdot 7H_2O$ by $NaBH_4$ (Shandong Ekes Chemical Technology Co., Ltd., Weifang, China) in the presence of CMC (M.W. 90,000, Macklin, Shanghai, China) as a stabilizer, following the established procedure [9,26]. Briefly, a CMC/Fe^{2+} precursor solution ([CMC]/[Fe^{2+}] = 1.54×10^{-3}) was reduced by dropwise addition of $NaBH_4$ ([BH_4^-]/[Fe^{2+}] = 4.0) at 4 mL min^{-1} under continuous N_2 purging and ultrasonication to prevent aggregation. The resulting CNZVI suspension (~8.3 g L^{-1}) was diluted to 300 mg L^{-1} with 1 mM NaCl background solution. The nanoparticles were collected using the magnetic absorption method, followed by sequential washing with anhydrous ethanol and ultrapure water, and then transferred to a Petri dish. After pre-freezing in a refrigerator at −80 °C for 1 h, the nanoparticles were dried using a vacuum freeze dryer and stored under vacuum. Subsequently, the morphology of CNZVI was analyzed using scanning electron microscopy. The particles were quasi-spherical (primary diameter 50–100 nm) with a hydrodynamic diameter of 300 ± 20 nm and a zeta potential of −30 ± 5 mV, as measured by dynamic light scattering (DLS) and electrophoretic mobility using a Zetasizer Nano ZS90 (Malvern Panalytical Ltd., Malvern, UK). Good colloidal stability of the CNZVI prepared by this method has been verified previously [26]. The CNZVI suspension was used within 2 h after preparation to preserve particle reactivity.

2.2. Humic Acid Size Fractions

Stock solutions of humic acid (HA, Sigma-Aldrich, St. Louis, MO, USA) at 60 mg L^{-1} were prepared in Tris-HCl buffer (pH 7.6 ± 0.1, containing 1 mM NaCl). The HA solution was sequentially filtered through polypropylene syringe filters (Jinteng Technology, Tianjin, China) with decreasing pore sizes of 1, 0.45, and 0.1 μm, yielding three distinct HA filtrates. The filtrate containing HA all smaller than 1 μm was designated as $HA_{1\mu m}$, that containing HA all smaller than 0.45 μm was designated as $HA_{0.45\mu m}$, and that containing HA all smaller than 0.1 μm was designated as $HA_{0.1\mu m}$. The concentration of HA in each filtrate was determined at 254 nm using a UV-visible spectrophotometer (U-2910, Hitachi, Ltd., Tokyo, Japan). The zeta potentials of the three HA size fractions were measured in triplicate at 25 °C using a Zetasizer Nano ZS90.

The hydrophobicity of each HA fraction was assessed by the partitioning of NOM between two immiscible phases [27]: 4 mL of HA solution was mixed with 1 mL of n-dodecane (≥99%, Macklin, Shanghai, China), vortexed for 2 min, and allowed to stand for 15 min for phase separation.

2.3. Porous Medium

Iron oxide-coated quartz sand (IOCS) was used as the porous medium. Quartz sand (analytical grade, Damao Chemical Reagent, Tianjin, China) was sieved to collect the 0.14–0.22 mm size fraction. Iron oxide coating was performed according to Yang et al. [16]. Briefly, the clean sand was immersed in 1.5 M $FeCl_3$ (analytical grade, Aladdin, Shanghai, China) for 30 min, dried at 35 °C for 2–3 h, and then submerged in 3 M NH_4OH (analytical grade, Hengxing Reagent, Tianjin, China) to precipitate surface-associated iron ions. Soak for 30 min and dry overnight at 60 °C. Finally, ultrasonic washing of the coated sand was carried out in deionized water to remove the loosely bonded iron oxides and impurities.

2.4. Experimental Solutions

All solutions were prepared with ultrapure water (≥18.2 MΩ cm, Milli-Q, Millipore, Burlington, MA, USA). The background solution consisted of 1 mM NaCl and Tris-HCl buffer, maintaining pH at 7.6 ± 0.1. All solutions were degassed under vacuum for 15 min prior to use.

2.5. Mixing Experiments with CNZVI and HA

A 300 mg L^{-1} CNZVI suspension was mixed at a 1:1 volume ratio with either the background solution or a 20 mg L^{-1} HA solution of each size fraction. After 5 min of sonication, the zeta potential and hydrodynamic diameter of CNZVI were monitored over 2 h using a Zetasizer Nano ZS90 to evaluate the effect of HA on CNZVI colloidal stability.

2.6. Column Transport Experiments

Chromatography columns (C10/10, 1.0 cm inner diameter, GE Healthcare, Piscataway, NJ, USA) were wet-packed with a 3 cm layer of IOCS using an ultrasonic-assisted method [26]. The mean column porosity, determined gravimetrically, was 0.43, corresponding to a pore volume (PV) of 1.01 mL. Wall effects were considered negligible given a column-to-grain-diameter ratio exceeding 45. Each packed column was initially flushed with background solution at 3 mL min^{-1} for 30 min to stabilize the system and remove residual air bubbles.

As shown in Figure 1, CNZVI and HA (or background solution, for controls) were co-injected using a peristaltic pump (BT100F, Lead Fluid Technology, Baoding, Beijing, China) coupled to an eight-port valve. During co-injection, the CNZVI stock suspension was continuously stirred under N_2 to maintain uniform dispersion and prevent oxygen contact. The column effluent was directed through PTFE tubing to a UV flow-through cell, and absorbance at 508 nm was monitored continuously online at 10 s intervals using a UV–visible spectrophotometer (U-2910, Hitachi, Ltd., Tokyo, Japan). Absorbance was converted to CNZVI concentration using a pre-established calibration curve.

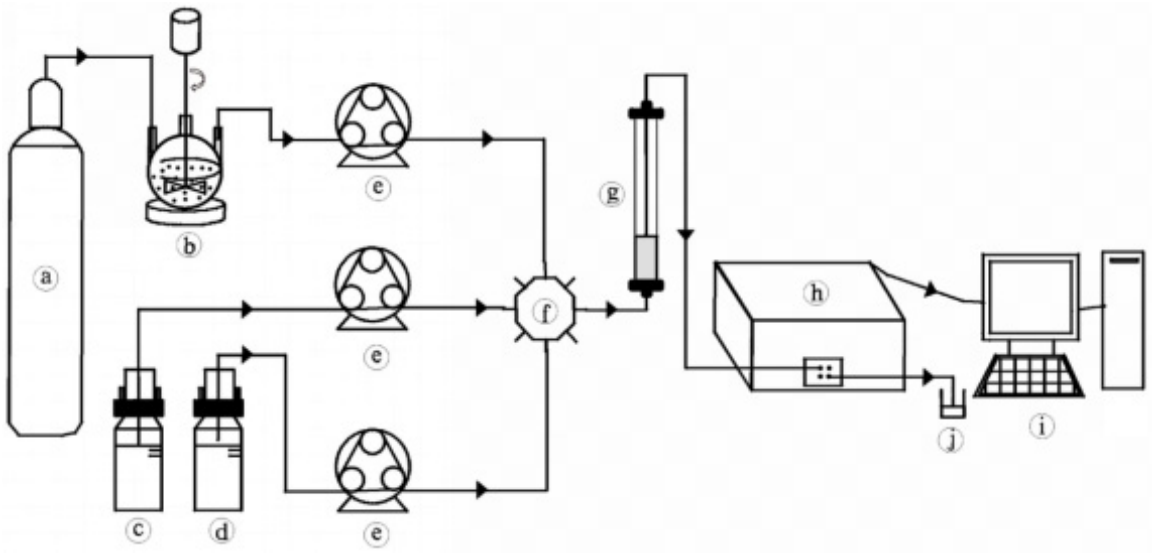

Figure 1. Schematic illustration of the experimental setup: (**a**) Nitrogen gas, (**b**) CNZVI reservoir, (**c**) Flushing solution reservoir, (**d**) Humic acid reservoir, (**e**) Peristaltic pump × 3, (**f**) Switch valve, (**g**) Sand columns, (**h**) UV-Vis spectrophotometer, (**i**) Computer, and (**j**) Effluent collector.

Two experimental groups were set up, including seven independent column chromatography transport experiments, each experiment was repeated at least three times:

(1) Particle-size-effect set (total injection flow rate = 1 mL min^{-1}): (a) CNZVI + background solution (control; no HA); (b) CNZVI + $HA_{1\mu m}$ (co-injection; HA = 60 mg L^{-1}); (c) CNZVI + $HA_{0.45\mu m}$ (co-injection; HA = 60 mg L^{-1}); and (d) CNZVI + $HA_{0.1\mu m}$ (co-injection; HA = 60 mg L^{-1}). Co-injection was maintained for 10 min, with each solution delivered at 0.5 mL min^{-1}. The eight-port valve was then switched to the background-solution channel, and the column was flushed at 1 mL min^{-1} for 10 min to elute unretained CNZVI particles.

(2) Flow-rate-effect set (total injection flow rate = 2 mL min^{-1}): (a) CNZVI + background solution (control; 2 mL min^{-1}); (b) CNZVI + $HA_{1\mu m}$ at the high flow rate (co-injection; HA = 60 mg L^{-1}); and (c) CNZVI + $HA_{0.1\mu m}$ at the high flow rate (co-injection; HA = 60 mg L^{-1}). Co-injection was maintained for 5 min, with each solution delivered at 1 mL min^{-1}. The column was subsequently flushed at 2 mL min^{-1} for 5 min.

2.7. Data Analysis

Breakthrough curves (BTCs) were obtained by plotting the ratio of effluent to influent CNZVI concentration (C/C_0) as a function of time expressed in pore volumes (PVs). The deposition rate (K_d) was calculated from the relative effluent concentration at the initial breakthrough point using [28].

$$K_d = -\frac{v}{\varepsilon L}\ln\left(\frac{C}{C_0}\right) \quad (1)$$

where v is the pore-water velocity (cm min^{-1}), L is the packed-bed height (3 cm), ε is the porosity (0.43), and C/C_0 is the relative CNZVI effluent concentration at the initial breakthrough point. A larger K_d indicates stronger nanoparticle deposition and lower mobility.

The maximum transport distance (L_T) was calculated by the following two formulas. First, use formula 2 [29] to calculate Single Collector Efficiency η, and then substitute it into formula 3 [30] to obtain the maximum migration distance.

$$\eta = -\frac{2d_c}{3L(1-\varepsilon)}\ln\left(\frac{c}{c_0}\right) \quad (2)$$

$$L_T = -\ln\left(\frac{C_L}{C_0}\right)\left(\frac{2d_c}{3(1-\varepsilon)\eta}\right) \quad (3)$$

where d_c is the sand diameter, L, ε and C/C_0 are consistent with the formula 1, and C_L/C_0 is the fixed value of 0.001.

The maximum transport distance ratio (L_{T1}/L_{T2}) under different experimental conditions was quantified from the relative change in collision efficiency (α_2/α_1) [30].

$$\frac{L_{T2}}{L_{T1}} = \frac{\alpha_1}{\alpha_2} = \frac{\ln\left(\frac{C_1}{C_0}\right)}{\ln\left(\frac{C_2}{C_0}\right)} \quad (4)$$

To quantify the relative importance of HA size and injection flow rate in controlling CNZVI transport, a 2 × 2 factorial design approach [20] was used to calculate the main effect (ME) of each factor and the two-factor interaction factor (IF). The ME represents the change in response (K_d) when a factor is shifted from one level to another; a larger absolute ME indicates a stronger effect, whereas an ME approaching zero indicates little or no effect. The IF represents the magnitude of the coupled effect; an IF approaching zero indicates the absence of interaction and an approximately additive response, whereas a larger absolute IF indicates stronger interaction. Figures were generated using Origin 2024 software.

3. Results

3.1. Zeta Potential of Humic Acid

Zeta potentials of the three humic acid (HA) fractions are shown in Figure 2. The three fractions, respectively $HA_{1\mu m}$, $HA_{0.45\mu m}$, and $HA_{0.1\mu m}$, demonstrated comparable zeta potential values of −35 ± 5 mV. This suggests that the differences in the organic effect on CNZVI transport should not be attributed to the differences in charge properties of the humic acid.

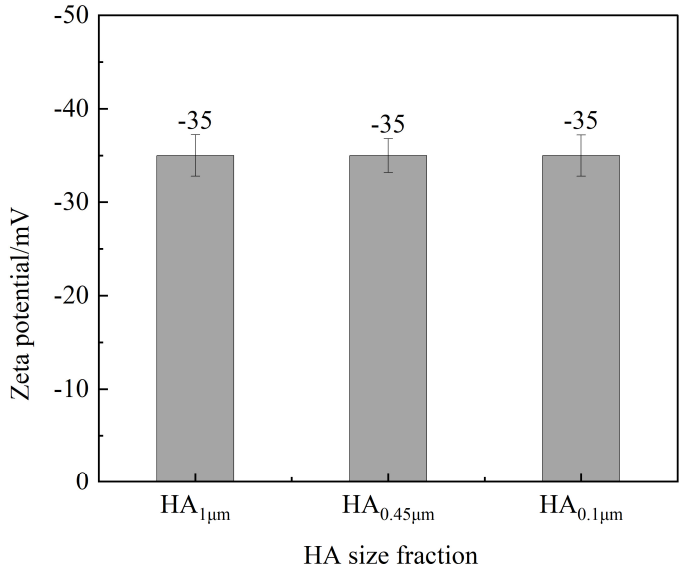

Figure 2. Zeta potentials of the different HA size fractions.

3.2. Scanning Electron Microscope (SEM) Analysis of NZVI and CNZVI

Figure 3 compares the SEM images of NZVI and CNZVI. The NZVI particles exhibited smooth surfaces and were clustered into short chain-like structures (Figure 3A,B), suggesting an aggregated state. In contrast, the CNZVI particles displayed rougher surfaces and quasi-spherical shapes with diameters ranging from 50 to 100 nm (Figure 3C,D), suggesting that CMC was successfully coated onto the NZVI particles, resulting in improved colloidal stability.

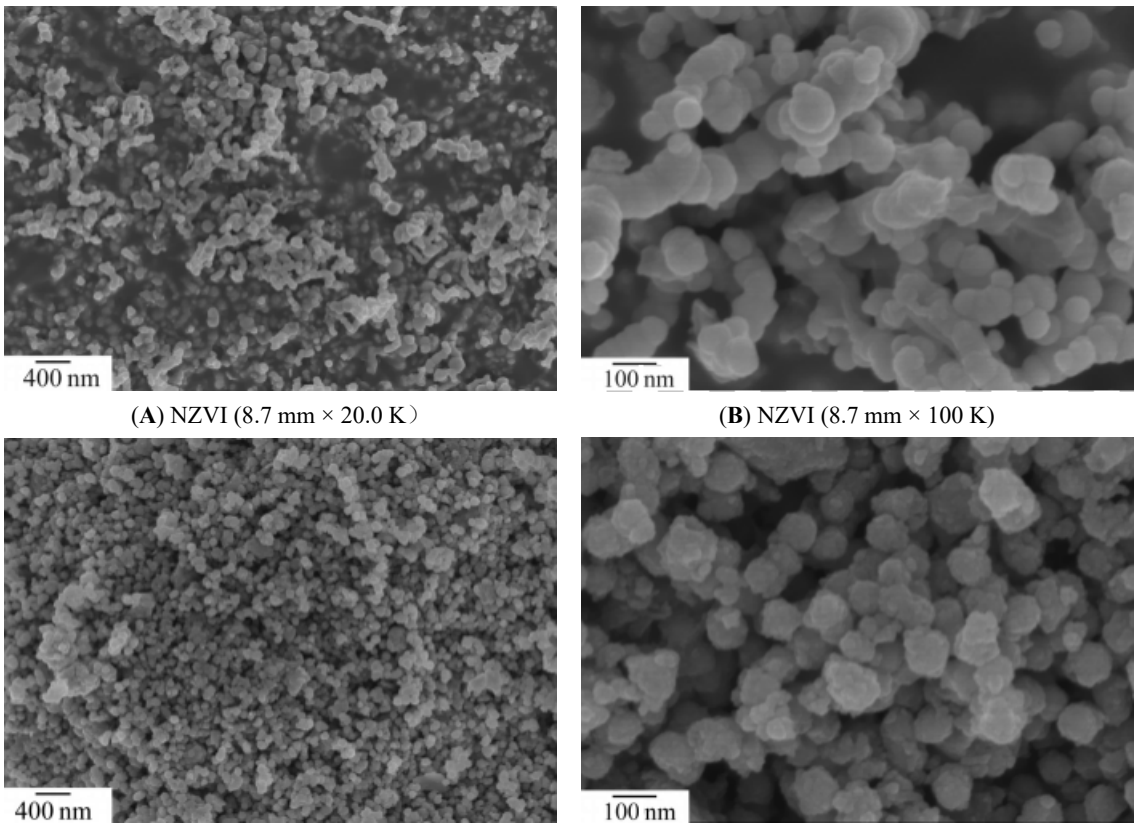

(**A**) NZVI (8.7 mm × 20.0 K） (**B**) NZVI (8.7 mm × 100 K)

(**C**) CNZVI (8.7 mm × 20.0 K) (**D**) CNZVI (8.7 mm × 100 K)

Figure 3. Scanning electron micrographs of NZVI and CNZVI. (**A**,**B**) NZVI particles; (**C**,**D**) CNZVI particles.

3.3. Insignificant Effect of HA on the Particle Size and Zeta Potential of CNZVI

Figure 4 shows the particle size and zeta potential of CNZVI in the absence and presence of HA. Figure 4A shows the hydrodynamic diameter of CNZVI remained at about 300 ± 20 nm with/out HA, suggesting insignificant

impact of HA on the particle size of CNZVI. Figure 4B shows that introduction of HA induced insignificant change in zeta potential, which remained at about −30 ± 5 mV. These results suggest that little HA was adsorbed onto CNZVI surfaces. Thusly, any change in CNZVI mobility in the presence of HA, as observed in the next Section shall not be attributed to CNZVI surface modification by HA.

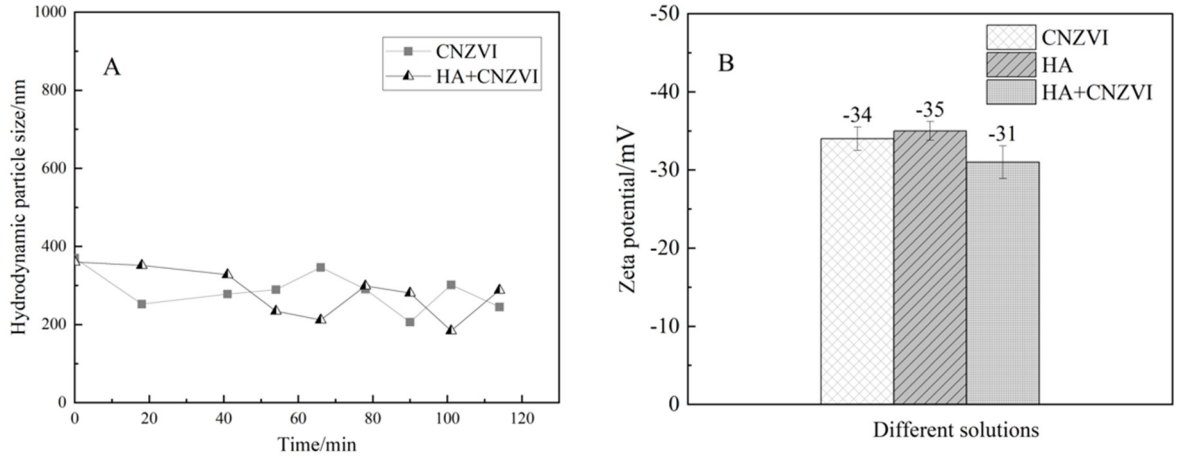

Figure 4. Effects of HA on the particle size (**A**) and zeta potential (**B**) of CNZVI.

3.4. Influence of HA on CNZVI Transport

Figure 5 summarizes the breakthrough curves (BTCs) of CNZVI, under the influence of co-injected HA. Table 1 lists the corresponding deposition rates and maximum transport of CNZVI. The elevation of the inflection points decreased from about 0.59 to 0.41 as the size of the co-injected HA increased from 0.1 to 1 μm. Table 1 shows that this corresponds to an increasing K_d from 0.52 min^{-1} to 0.88 min^{-1}. Under the impact of $HA_{1\mu m}$, the maximum transport distance (L_T) of the CNZVI was 23 cm. The L_T increased to 32 cm for $HA_{0.45\mu m}$, and to 39 cm for $HA_{0.1\mu m}$. This suggests that the L_T for $HA_{0.45\mu m}$ and $HA_{0.1\mu m}$ are approximately 1.39 times and 1.70 times that of $HA_{1\mu m}$, respectively. In conclusion, lower-sized HA was more effective in promoting CNZVI transport than the higher-sized HA.

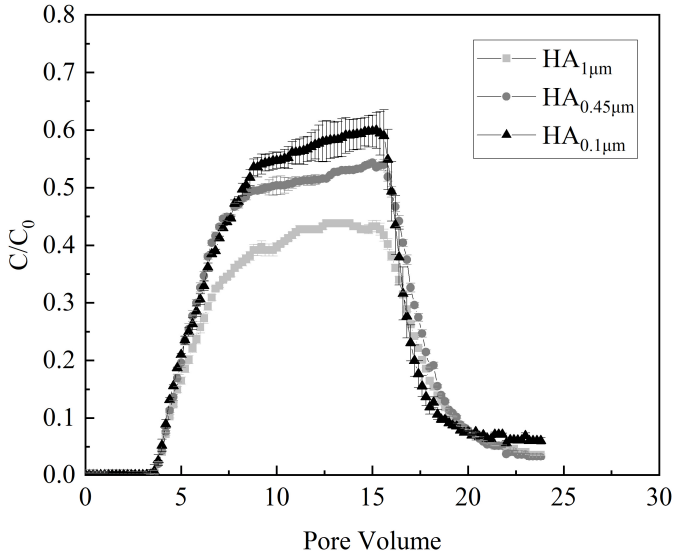

Figure 5. Effect of HA size on CNZVI transport.

Table 1. Size-dependent influence of HA on the deposition rate and maximum transport distance of CNZVI through iron oxide-coated sand (flow rate = 1 mL min^{-1}).

HA Class	Deposition Rate K_d (min^{-1})	Maximum Transport Distance L_T (cm)
$HA_{1\mu m}$	0.88	23
$HA_{0.45\mu m}$	0.65	32
$HA_{0.1\mu m}$	0.52	39

Previously, we investigated the transport of large and small latex microspheres (50 nm and 200 nm) in the same IOCS porous medium at a fixed HA size (~2 nm) [20]. We found that at a fixed HA size, increasing the particle size of latex microspheres led to reduced deposition rate and increased maximum transport distance. In this study, we further noted that at a fixed nanoparticle size, decreasing the HA size also led to reduced deposition rate and increased maximum transport distance. Based on the two studies, we could reasonably speculate that by increasing the colloid-to-OM size ratio, the site blocking effect and mobility-promoting effect of the OM on the colloid could be enhanced, no matter if the size ratio was achieved by increasing the colloid size or decreasing the organic matter size. This speculation was validated with both the organic plastic material and the inorganic iron material. This implies that in nanoremediation operation, the mobility of the nano-agent could be improved by using either the larger-sized nano-agent of smaller-sized humic acid (for nanoparticle site blockage). No explicit functional relationship between the size ratio and particle deposition rate was observed based on these two studies. Further studies to make more data available would be conducive to resolve this issue.

3.5. Coupled Effects of HA Size and Flow Rate on CNZVI Transport

Figure 6 summarizes the BTCs of CNZVI at different flow rates under the influence of different-sized HA. For both the large and small HA, higher CNZVI effluent concentrations were recorded on the BTCs. When CNZVI was co-injected with $HA_{1\mu m}$, increasing the flow rate from 1 to 2 mL min^{-1} increased C/C_0 by 46.3% (from 0.41 to 0.60); while for the $HA_{0.1\mu m}$, increasing the flow rate over the same range increased C/C_0 by 18.6% (from 0.59 to 0.70). This suggests higher CNZVI mobility at higher flow rate.

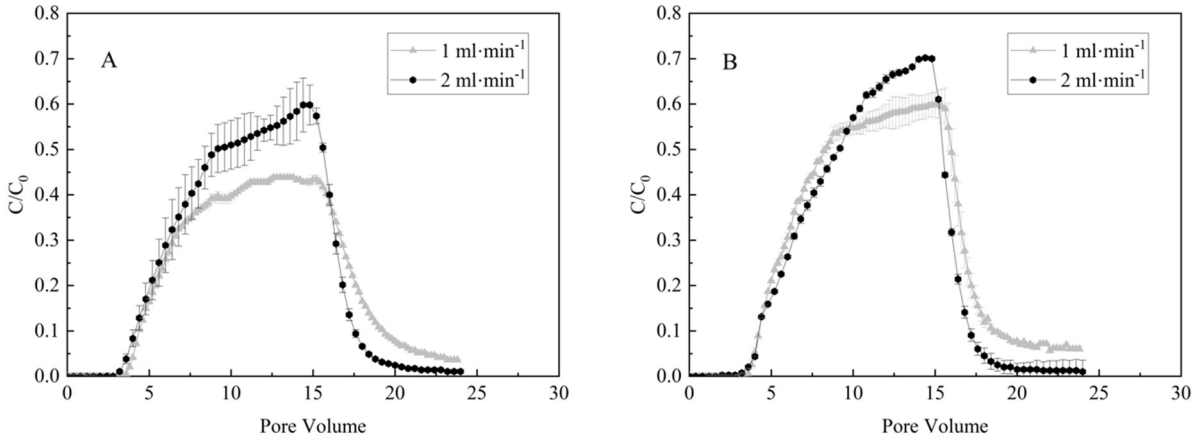

Figure 6. Coupled effects of flow rate and HA size: (**A**) effect of flow rate on CNZVI transport in the presence of large HA ($HA_{1\mu m}$); (**B**) effect of flow rate on CNZVI transport in the presence of small HA ($HA_{0.1\mu m}$).

Table 2 lists the deposition rate and maximum transport distance of CNZVI under the coupled influence of humic acid and flow rate. The maximum transport distance of CNZVI at a flow rate of 2 mL min^{-1} was 1.78 times that observed at 1 mL min^{-1} in the presence of $HA_{1\mu m}$, whereas only a 1.49-fold increase was recorded with $HA_{0.1\mu m}$. These results suggest that the larger HA fraction was more effective at facilitating CNZVI mobility under elevated flow conditions (L_T ratio: 1.78 vs. 1.49).

Table 2. Coupled effects of HA size and flow rate on CNZVI deposition rate and maximum transport distance through iron oxide-coated sand.

HA Class	Flow Rate (mL min^{-1})	Deposition Rate K_d (min^{-1})	Maximum Transport Distance L_T (cm)
$HA_{1\mu m}$	1	0.88	23
	2	1.01	41
$HA_{0.1\mu m}$	1	0.52	39
	2	0.70	58

The greater CNZVI mobility at the higher flow rate can be explained with our previously identified mechanisms. The shadow zone formed downstream a deposited particle is expanded at higher flow rate [20,31]. Consequently, the effective site area occupied by the particle (physical footprint of the particle plus the shadow zone) increased with increasing flow rate. In other words, increasing flow rate led to increasing ratio of particle-

occupied site area to the HA size. Based on our previous findings, this could increase the mobility-promoting effect of the HA. On the other hand, based on the available data we are unable to explain why the flow rate-associated mobility-promoting effect was more pronounced for the larger than the smaller sized HA.

3.6. Main Effects and Interaction of HA Size and Flow Rate

The relative importance of flow rate and HA size in controlling nanoparticle transport was quantified using the main effect (ME), defined as the change in the response caused by shifting a factor from one level to another. A larger absolute value denotes a stronger effect, whereas zero denotes no effect. After calculation, the ME of HA size was −0.33 and that of flow rate was −0.16, indicating that HA size was the dominant control on CNZVI transport.

The interaction between flow rate and HA size was quantified using the interaction factor (IF). A value of zero indicates no interaction or an additive response [20]. After calculation, an IF of −0.03 was obtained, indicating a weak antagonistic interaction between HA size and flow rate.

4. Conclusions

The core finding of this study is that co-injection of humic acid with zero valent-iron can increase the mobility of the iron nanoparticle. The mobility promoting effect of HA could be maximized using lower HA and higher flow rate. Integrating these results with our previous work [20], we observed that the HA-induced mobility enhancement can be intensified by either increasing the nanoparticle size or decreasing the HA size, as both approaches increase the particle-to-HA size ratio. The size ratio can also be raised by applying higher flow rates. Our study thusly identified the particle-to-HA size ratio as a critical parameter that could guide the delivery operation in contaminated groundwater remediation.

Zero-valent iron nanoparticles are a class of engineered nanomaterials used for *in situ* remediation of contaminated groundwater. However, their limited mobility remains a critical bottleneck, constraining both the efficiency and practical applicability of this remediation approach. Our findings offer a preliminary strategy to address this limitation. Future research should aim to establish a quantitative relationship between the deposition rate (or maximum transport distance) of NZVI and the particle-to-HA size ratio, which would enable more precise and controllable application of this technology.

Author Contributions

T.C.: conceptualization, methodology, software, visualization, writing—original draft; Y.W.: investigation, software, validation, data curation; X.Y.: supervision, writing—review & editing, methodology, funding acquisition, resources, project administration. All authors have read and agreed to the published version of the manuscript.

Funding

This research was funded by the National Natural Science Foundation of China (42177406).

Institutional Review Board Statement

Not applicable.

Informed Consent Statement

Not applicable.

Data Availability Statement

The data presented in this study are available on request from the corresponding authors.

Conflicts of Interest

The authors declare no conflict of interest.

Use of AI and AI-Assisted Technologies

During the preparation of this work, the authors used ChatGPT for language polishing. After using this tool, the authors reviewed and edited the content as needed and take full responsibility for the content of the published article.

References

1. Chen, H.; Qian, L. Performance of field demonstration nanoscale zero-valent iron in groundwater remediation: A review. *Sci. Total Environ.* **2024**, *912*, 169268. https://doi.org/10.1016/j.scitotenv.2023.169268.
2. Pandey, K.; Sharma, S.; Saha, S. Advances in design and synthesis of stabilized zero-valent iron nanoparticles for groundwater remediation. *J. Environ. Chem. Eng.* **2022**, *10*, 107993. https://doi.org/10.1016/j.jece.2022.107993.
3. Guo, A.; Yu, H.; Li, T.; et al. Mechanistic and Engineering Perspectives on Coupled Nanoscale Zero-Valent Iron-Organohalide-Respiring Bacteria Remediation of Trichloroethylene-Contaminated Groundwater. *Remediat. Ecol.* **2026**, *1*, 3.
4. Ahn, J.Y.; Kim, C.; Jun, S.C.; et al. Field-scale investigation of nanoscale zero-valent iron (NZVI) injection parameters for enhanced delivery of NZVI particles to groundwater. *Water Res.* **2021**, *202*, 117402. https://doi.org/10.1016/j.watres.2021.117402.
5. Asad, M.A.; Khan, U.T.; Krol, M.M. Subsurface transport of carboxymethyl cellulose (CMC)-stabilized nanoscale zero valent iron (nZVI): Numerical and statistical analysis. *J. Contam. Hydrol.* **2021**, *243*, 103870. https://doi.org/10.1016/j.jconhyd.2021.103870.
6. Mondal, A.; Dubey, B.K.; Arora, M.; et al. Porous media transport of iron nanoparticles for site remediation application: A review of lab scale column study, transport modelling and field-scale application. *J. Hazard. Mater.* **2021**, *403*, 123443. https://doi.org/10.1016/j.jhazmat.2020.123443.
7. Xie, Y.; Zhang, M.; Ma, L.; et al. Overlooked encounter process that affects physical behaviors of stabilized nanoscale zero-valent iron during *in situ* groundwater remediation. *J. Hazard. Mater.* **2024**, *461*, 132547. https://doi.org/10.1016/j.jhazmat.2023.132547.
8. Sackey, E.A.; Yang, X. Synergistic adsorption and reductive degradation of Congo Red dye by polyvinylpyrrolidone-stabilized nanoscale zero-valent iron. *Surf. Interfaces* **2026**, *95*, 109805. https://doi.org/10.1016/j.surfin.2026.109805.
9. He, F.; Zhao, D. Manipulating the Size and Dispersibility of Zerovalent Iron Nanoparticles by Use of Carboxymethyl Cellulose Stabilizers. *Environ. Sci. Technol.* **2007**, *41*, 6216–6221. https://doi.org/10.1021/es0705543.
10. Saleh, N.; Kim, H.J.; Phenrat, T.; et al. Ionic Strength and Composition Affect the Mobility of Surface-Modified Fe^0 Nanoparticles in Water-Saturated Sand Columns. *Environ. Sci. Technol.* **2008**, *42*, 3349–3355. https://doi.org/10.1021/es071936b.
11. Tiraferri, A.; Sethi, R. Enhanced transport of zerovalent iron nanoparticles in saturated porous media by guar gum. *J. Nanopart. Res.* **2009**, *11*, 635–645. https://doi.org/10.1007/s11051-008-9405-0.
12. Xin, J.; Tang, F.; Zheng, X.; et al. Transport and retention of xanthan gum-stabilized microscale zero-valent iron particles in saturated porous media. *Water Res.* **2016**, *88*, 199–206. https://doi.org/10.1016/j.watres.2015.10.005.
13. Luo, T.; Pokharel, R.; Chen, T.; et al. Fate and Transport of Pharmaceuticals in Iron and Manganese Binary Oxide Coated Sand Columns. *Environ. Sci. Technol.* **2023**, *57*, 214–221. https://doi.org/10.1021/acs.est.2c05963.
14. Choe, Y.; Won, J.; Burns, S.E. Impact of particle size and oxide phase on microplastic transport through iron oxide-coated sand. *Water Res.* **2025**, *271*, 122856. https://doi.org/10.1016/j.watres.2024.122856.
15. Wang, D.; Bradford, S.A.; Harvey, R.W.; et al. Humic Acid Facilitates the Transport of ARS-Labeled Hydroxyapatite Nanoparticles in Iron Oxyhydroxide-Coated Sand. *Environ. Sci. Technol.* **2012**, *46*, 2738–2745. https://doi.org/10.1021/es203784u.
16. Yang, X.; Flynn, R.; von der Kammer, F.; et al. Quantifying the influence of humic acid adsorption on colloidal microsphere deposition onto iron-oxide-coated sand. *Environ. Pollut.* **2010**, *158*, 3498–3506. https://doi.org/10.1016/j.envpol.2010.03.011.
17. Chen, B.; Lv, N.; Xu, W.; et al. Transport of nanoscale zero-valent iron in saturated porous media: Effects of grain size, surface metal oxides, and sulfidation. *Chemosphere* **2023**, *313*, 137512. https://doi.org/10.1016/j.chemosphere.2022.137512.
18. Yang, X.; Flynn, R.; von der Kammer, F.; et al. Influence of ionic strength and pH on the limitation of latex microsphere deposition sites on iron-oxide coated sand by humic acid. *Environ. Pollut.* **2011**, *159*, 1896–1904. https://doi.org/10.1016/j.envpol.2011.03.026.
19. Yang, X.; Deng, S.; Wiesner, M.R. Comparison of enhanced microsphere transport in an iron-oxide-coated porous medium by pre-adsorbed and co-depositing organic matter. *Chem. Eng. J.* **2013**, *230*, 537–546. https://doi.org/10.1016/j.cej.2013.06.122.
20. Yang, X.; Zhang, Y.; Chen, F.; et al. Interplay of Natural Organic Matter with Flow Rate and Particle Size on Colloid Transport: Experimentation, Visualization, and Modeling. *Environ. Sci. Technol.* **2015**, *49*, 13385–13393. https://doi.org/10.1021/acs.est.5b02972.
21. Dangi, M.B.; Urynowicz, M.A.; Schultz, C.L.; et al. A comparison of the soil natural oxidant demand exerted by permanganate, hydrogen peroxide, sodium persulfate, and sodium percarbonate. *Environ. Chall.* **2022**, *7*, 100456. https://doi.org/10.1016/j.envc.2022.100456.
22. Li, X.; Wu, B.; Zhang, Q.; et al. Mechanisms on the impacts of humic acids on persulfate/Fe^{2+}-based groundwater remediation. *Chem. Eng. J.* **2019**, *378*, 122142. https://doi.org/10.1016/j.cej.2019.122142.

23. Ratpukdi, T.; Intarasuwan, K.; Jutaporn, P.; et al. Interactions between natural organic matter fractions and nanoscale zero-valent iron. *Sci. Total Environ.* **2021**, *796*, 148954. https://doi.org/10.1016/j.scitotenv.2021.148954.
24. Liu, Z.; Fu, J.; Liu, A.; et al. Influence of natural organic matter on nanoscale zero-valent iron for contaminants removal in water: A critical review. *Chem. Eng. J.* **2024**, *488*, 150836. https://doi.org/10.1016/j.cej.2024.150836.
25. Cui, R.; Ye, X.; Du, X. Coupled effects of bacteria and suspended solids on clogging during managed aquifer recharge. *J. Hydrol.* **2021**, *600*, 126543. https://doi.org/10.1016/j.jhydrol.2021.126543.
26. Wu, W.; Han, L.; Nie, X.; et al. Effects of multiple injections on the transport of CMC-nZVI in saturated sand columns. *Sci. Total Environ.* **2021**, *784*, 147160. https://doi.org/10.1016/j.scitotenv.2021.147160.
27. Wang, J.; Ding, S.; Liu, K.; et al. High-Throughput Method for Natural Organic Matter Hydrophobicity Assessment Using an Ionic Liquid-Based Aqueous Two-Phase System. *Environ. Sci. Technol.* **2021**, *55*, 13953–13960. https://doi.org/10.1021/acs.est.1c04436.
28. Kretzschmar, R.; Barmettler, K.; Grolimund, D.; et al. Experimental determination of colloid deposition rates and collision efficiencies in natural porous media. *Water Resour. Res.* **1997**, *33*, 1129–1137. https://doi.org/10.1029/97wr00298.
29. Xiong, X.; Yang, Z.; Hu, R.; et al. Evaluating Single-Collector Efficiencies of Colloid Deposition from Lagrangian Simulations: Geometric Models and Particle Release Scenarios. *Water Resour. Res.* **2022**, *58*, e2022WR033821. https://doi.org/10.1029/2022wr033821.
30. Elimelech, M. *Particle Deposition and Aggregation: Measurement, Modelling, and Simulation*; Butterworth-Heinemann: Oxford, UK; Boston, MA, USA, 1995; pp. 368–375.
31. Ko, C.H.; Elimelech, M. The "Shadow Effect" in Colloid Transport and Deposition Dynamics in Granular Porous Media: Measurements and Mechanisms. *Environ. Sci. Technol.* **2000**, *34*, 3681–3689. https://doi.org/10.1021/es0009323.